Journal of Alloys and Compounds 978 (2024) 173483

Contents lists available at ScienceDirect

Journal of Alloys and Compounds

journal homepage: www.elsevier.com/locate/jalcom

High-pressure properties of thallium orthovanadate from density-functional theory calculations

T. Ouahrani [a,b,*], A. Muñoz [c], R. Franco [d], R.M. Boufatah [b], Z. Bedrane [b], D. Errandonea [e,**]

[a] École Supérieure en Sciences Appliquées, ESSA-Tlemcen, BB 165 RP Bel Horizon, Tlemcen 13000, Algeria
[b] Laboratoire de Physique Théorique, Université de Tlemcen, BP 119, 13000, Algeria
[c] Departamento de Física, MALTA-Consolider Team, Instituto de Materiales y Nanotecnología, Universidad de La Laguna, San Cristóbal de La Laguna, E38200 Tenerife, Spain
[d] MALTA Consolider Team and Departamento de Química Física y Analítica, Universidad de Oviedo, E-33006 Oviedo, Spain
[e] Departamento de Física Aplicada - Instituto de Ciencia de Materiales, MALTA Consolider Team, Universidad de Valencia, Edificio de Investigación, C/Dr. Moliner 50, Burjassot 46100, Valencia, Spain

ARTICLE INFO

Keywords:
Ab initio calculations
Phase transitions
High pressure
Pressure-induced amorphization
Band structure

ABSTRACT

Thallium vanadate is the missing piece to fully understand the behavior of orthovanadates under high-pressure conditions. Here we report a computational study of $TlVO_4$ under high pressure. Its properties and stability have been studied using the density-functional theory. We have found that $TlVO_4$ undergoes at 2.7 GPa a phase transition from the $CrVO_4$-type structure (described by space group *Cmcm*) to a wolframite-type structure (described by space group *P2/c*). In contrast to the behavior of isomorphic vanadates, a subsequent amorphization takes place beyond 6 GPa being it driven by dynamic instabilities. In addition to the structural analysis, we present a systematic study of elastic, vibrational, and bonding properties, as well as a characterization of the electronic band structure and electronic density of states. The distinctive behavior of $TlVO_4$ is attributed to the contribution to the bonding of Tl 6*s* states. The implications of the observed phase transition and amorphization will be discussed.

1. Introduction

During the last decade, a large number of studies on orthovanadate AVO_4 compounds have been conducted to investigate their high-pressure behavior. In most of these studies, it has been shown that VO_4 tetrahedral units, characteristic of the crystal structure of orthovanadates, played a critical role in their high-pressure structural sequence [1]. Of particular interest are compounds crystallizing in the $CrVO_4$-type structure, described by space group (S.G.) *Cmcm* [2], and often also called $NiSO_4$-type structure. These compounds include $TlVO_4$. In $CrVO_4$-type compounds, the VO_4 tetrahedral units are vulnerable to coordination changes, which results in phase transitions and drastic modifications in the electronic and vibrational properties. Information on the high-pressure behavior of compounds isostructural to $CrVO_4$ is of particular relevance because the crystal structure is shared by more than thirty different ternary oxides, including not only vanadates, but also sulfates, chromates, phosphates, and selenates [3]. In addition, given the close connection of the $CrVO_4$-type structure with quartz-like oxides [4], a high-pressure study of the structural, vibrational, and properties of a compound like $TlVO_4$ is quite attractive from the fundamental point of view.

Structural changes induced by pressure on $CrVO_4$-type vanadates are highly dependent on the trivalent cation *A* [2,5,6]; for instance, In, Fe, or Cr. In particular, it has been shown that $FeVO_4$, $InVO_4$, and $CrVO_4$ follow two different structural sequences [2,5,6]. The phase transitions are from the orthorhombic polymorph (S.G. *Cmcm*), represented in Figure S1 of the Supplementary Material (S.M.) [7], which has a low-packing efficiency and it is formed by chains of nearly regular edge-sharing AO_6 octahedra linked together by VO_4 tetrahedra, to denser phases where V atoms are surrounded by six oxygen atoms in an octahedral coordination [5,6]. In the case of $InVO_4$ [8], several transitions have been reported, revealing a rich polymorphic sequence, which involves drastic changes in the interatomic In-O and V-O bond distances. In $InVO_4$ the sequence of phase transitions at 300 K is $CrVO_4$-type (S.G.

* Corresponding author at: École Supérieure en Sciences Appliquées, ESSA-Tlemcen, BB 165 RP Bel Horizon, Tlemcen 13000, Algeria.
** Corresponding author.
E-mail addresses: tarik_ouahrani@yahoo.fr (T. Ouahrani), daniel.errandonea@uv.es (D. Errandonea).

https://doi.org/10.1016/j.jallcom.2024.173483
Received 13 October 2023; Received in revised form 4 January 2024; Accepted 6 January 2024
Available online 10 January 2024

Cmcm) ⟶ wolframite-type (S.G. *P2/c*, at 4.4 GPa) ⟶ raspite-type (S.G. $P2_1/a$, at 28.1 GPa) ⟶ $AgMnO_4$-type (S.G. $P2_1/n$, at 44 GPa). In the case of $CrVO_4$ previous studies are limited to only 10 GPa [2], and only the $CrVO_4$-type (S.G. *Cmcm*) ⟶ wolframite (S.G. *P2/c*) phase transition has been reported at 4 GPa. In contrast, $FeVO_4$ has a more complex structural landscape with two-phase transitions reported below 4 GPa [6] being two triclinic structures observed at a lower pressure than the wolframite-type polymorph. The distinctive behavior of $FeVO_4$ has been proposed to be associated with the magnetic interaction between Fe atoms [9].

Pressure has been found to have a significant effect not only on the crystal structure of vanadates but also on the Raman and infrared (IR) phonon frequencies and on the branches of the phonon spectrum at the boundary of the Brillouin zone (BZ). This unusual trend and the results described in the previous paragraph prompted us to conduct additional research on $CrVO_4$-type vanadates, investigating for the first time, the high-pressure properties of $TlVO_4$. The interest in $TlVO_4$ has several motivations. After the synthesis reported by Touboul *et al.* [10,11], Butcher and coworkers [12] performed a photoelectrochemical characterization on this compound, revealing its potential as a photocatalytic material. On the other hand, photoluminescence measurements [12] determined a band gap of 2.94 eV, which is promising for water splitting and hydrogen evolution reaction processes. In addition, we expect lesser hybridization between Tl and O atoms than between In and O atoms. This is because trivalent thallium, in the octahedral coordination, has a larger Shannon radius, of 0.885 Å, than indium does, 0.800 Å [13]. As a result, different polymorphic sequences than in $InVO_4$ and $CrVO_4$ could occur in $TlVO_4$. On the other hand, due to this atomic configuration, the competition between energy, volume, and entropy changes can lead to instability during a pressure-induced phase transition. In fact, if the energy gain from the transition is not sufficient to compensate for the associated changes in volume and entropy, the transition may not occur smoothly. Instead, the system may exhibit intermediate or metastable states or even amorphization.

Additionally, when pressure is applied, the intermolecular or intramolecular forces between $TlVO_4$ constituents can be significantly altered. This change in pressure can influence the energy landscape of the substance and potentially destabilize its molecular or atomic structure. Indeed, the modification of intermolecular or intramolecular forces caused by pressure could facilitate chemical reactions between the constituents of the substance. These reactions may involve the breaking or forming of chemical bonds, resulting in the decomposition of the original phase. This scenario was observed by Touboul and coworkers [11]. Their work stipulates that at temperatures above 300 K $TlVO_4$ decomposes into $TlVO_3$ and 1/2 O_2. We would like to highlight here that, because Tl is very toxic, the preparation and experimental characterization of Tl-based materials have been poorly studied. To avoid experimental manipulation of such a compound, it is advantageous to investigate it first using theoretical tools. Therefore, to complete the understanding of $CrVO_4$-type vanadates under high pressure, we have decided to study $TlVO_4$ under high-pressure conditions by means of density-functional theory simulations.

2. Computational details

Zero-temperature total-energy calculations have been carried out within the framework of the density-functional theory (DFT) implemented in the Vienna Ab initio Simulation Package (VASP) [14–16]. The projector-augmented wave (PAW) method [17] has been employed to simulate the electronic band-structure calculations. The exchange-correlation energy has been described within generalized-gradient approximation (GGA) using the Perdew-Burke-Ernzerhof (PBE) functional [18,19] and also using the Armiento and Mattsson 2005 (AM05) functional [20]. A cutoff energy of 520 eV has been established for the plane waves after testing that it ensured the convergence of calculations. The traditional Monkhorst-Pack scheme [21] has been employed by using in the reciprocal space a dense grid of 10 × 10 × 7. In the relaxed equilibrium configuration, the forces have been found to be less than 0.3 meV/ Å per atom in each cartesian direction. Crystal structures have been optimized at fixed volumes. The pressure has been obtained from energy versus volume plots as the derivative of the total energy with respect to volume. The enthalpy (*H*) has been then obtained for each structure as $H = E + P \times V$.

Mechanical properties of the low- and high-pressure phases have been determined through the calculation of elastic constants, which have been obtained from the stress tensor which has been calculated when the relaxed structure is strained by changing its lattice vectors (magnitude and angle) using the stress-strain methodology implemented in VASP [22]. From the elastic constants, we have derived the different elastic moduli.

Lattice-dynamic calculations have been performed using the finite displacement method to calculate the interatomic force constants and obtain the phonon dispersion relations. This task requires the use in calculations of a 4 × 4 × 2 super-cell for $CrVO_4$-type (*Cmcm*) and a 4 × 2 × 4 super-cell for the high-pressure phase (*P2/c*), as well as constructing the force constant matrix, which contains the second derivatives of the total energy concerning the atomic displacements calculated within VASP, and extracting the vibrational modes through the open tool Phonopy [23,24]. This tool provides the irreducible representation of the modes at the Γ point. Combining these results with the SAM tool of the Bilbao Crystallographic Server we obtained the Raman, Infrared, and Silent modes.

We have also probed the bonding properties along the polymorphic sequence through the calculation of effective charges implemented in the Critic2 code [25]. The algorithm of this code is based on the topological analysis of scalar functions in real space based on the Quantum Theory of Atoms in Molecules (QTAIM) [26,27,29]. The code makes a topological partition into disjoint regions, providing the nature of interatomic bonds [28].

We have also calculated the formation energy of $TlVO_4$. It has been calculated at zero temperature and pressure without including the zero-point motion or lattice vibrations and following the formulation given in Refs. [30,31]. The total energy ($E(TlVO_4)$) of $TlVO_4$ per formula unit has been calculated as

$$E(TlVO_4) = E(Tl) + E(V) + 4E(O) + \Delta H(TlVO_4) \quad (1)$$

where $\Delta H(TlVO_4)$ is the formation enthalpy of $TlVO_4$, and E(i) is the energy of the constituent *i* elements; i.e. Tl, V, and O. Since

$$\Delta H(TlVO_4) = (\mu_{Tl} - E(Tl)) + (\mu_V - E(V)) + 4(\mu_O - E(O)) \quad (2)$$

Then

$$E(TlVO_4) = \Delta\mu_{Tl} + \Delta\mu_V + 4\Delta\mu_O \quad (3)$$

where μ_{Tl}, μ_V, and μ_O are respectively the chemical potentials of Tl, V, and O atoms. In our case, under thermal equilibrium growth conditions (constant temperature and pressure) $\mu_{TlVO_4} = E(TlVO_4)$.

In high-pressure calculations, based on crystal-chemistry arguments [32], in addition to the known orthorhombic polymorph of $TlVO_4$ ($CrVO_4$-type), we have considered as candidate structures the $MnMnO_4$-type structure (S.G. *C2/m*), the wolframite-type structure (S.G. *P2/c*), the post-wolframite structure reported in $CdWO_4$ (S.G. $P2_1/c$), the $AgMnO_4$-type structure (S.G. $P2_1/n$), the raspite-type structure (S.G. $P2_1/a$), the fergusonite-type structure (S.G. *C2/c*), the $HgWO_4$-type structure (S.G. *C2/c*), the $SrTeO_4$ structure (S.G. *Pbca*), the $BaUO_4$ structure (S.G. *Pbcm*), the zircon-type (S.G. $I4_1/amd$), the monazite-type structure (S.G. $P2_1/n$), and the scheelite-type structure (S.G. $I4_1/a$).

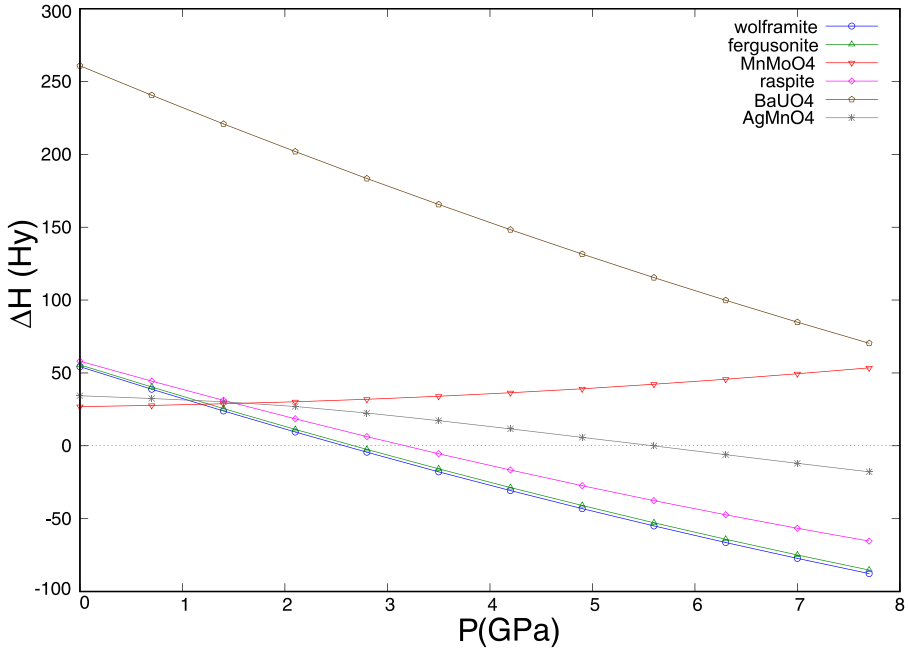

Fig. 1. (Color online) Pressure dependence of the enthalpy difference between different structures considered for $TlVO_4$ and the ambient-pressure structure ($CrVO_4$-type) which is represented by the horizontal dotted line at $\Delta H = 0$. The results correspond to AM05 calculations. For simplicity, we only show six structures in addition to the ambient pressure structure. The structures not represented have higher enthalpies than the structures included in the plot. The structures are identified by the names used in the description of calculations.

Table 1
Unit-cell parameters, volume at zero pressure (V_0), bulk modulus (B_0), and its pressure derivative ($B_0^{'}$) determined from this study for the ambient-pressure (*Cmcm*) and high-pressure (*P2/c*) polymorphs of $TlVO_4$.

	a (Å)	*b* (Å)	*c* (Å)	*β* (°)	V_0 (Å^3)	B_0 (GPa)	$B_0^{'}$
Cmcm (PBE)	5.901, 5.84*	8.916, 8.69*	7.016, 6.80*	90,90*	369.14	58.16	4.63
Cmcm (AM05)	5.842	8.822	6.939	90	357.62	58.31	4.09
P2/c (PBE)	4.950	5.856	5.086	92.24	147.32	114.56	4.62
P2/c (AM05)	4.894	5.767	5.026	92.42	141.73	131.09	4.14

The results calculated using two different functionals are given. For the ambient-pressure phase we compare the present with experiments from Ref. [11], The experimental results are denoted by the symbol *.

3. Results and discussion

3.1. Properties of $CrVO_4$-type at ambient-pressure

From calculations, after structural optimization of the internal atomic positions and lattice parameters, we have obtained the total energy as a function of volume and the enthalpy as a function of pressure for the different structures considered. The pressure has been determined by fitting the total energy versus volume results with a third-order Birch-Murnaghan equation of state (EOS) [33]. We have found that the structure with the lowest enthalpy at zero pressure is the stable orthorhombic polymorph of $TlVO_4$ (S.G. *Cmcm*), which has four formula units in the unit cell. This can be seen in Fig. 1 where we represent the calculated difference of enthalpy (using AM05) between different structures and the zero-pressure structure. The two functionals we have used lead to qualitatively similar enthalpy-pressure diagrams. The calculated unit-cell parameters of the stable structure are summarized in Table 1. The agreement with experiments [11] is good for the two functionals, being the best agreement obtained with AM05. From now on, when there are no specifications, we will refer to AM05 calculations. The calculated atomic coordinates are reported in Table S1 in the Supplementary Material [7]. These values are given for comparison with future studies since atomic positions have not yet been determined from experiments. The zero-pressure volume (V_0), bulk modulus (B_0), and its pressure derivative ($B_0^{'}$), obtained from the EOS, are also provided in Table 1. The bulk modulus, 58 GPa, is slightly smaller than values reported for the same parameter in isostructural $CrVO_4$ (63–93 GPa) and $InVO_4$ (69–76 GPa), in fergusonite-type $BiVO_4$ (62–84 GPa), and in the triclinic structure of $FeVO_4$ (76–80 GPa). On the other hand, the bulk modulus of $TlVO_4$ is considerably smaller than the same parameter in zircon-type and monazite-type orthovanadates, which have bulk moduli from 93 to 160 GPa [34]. Consequently, $TlVO_4$ is one of the most compressible orthovanadates.

To test a possible decomposition of $TlVO_4$, we have selected a number of decomposition routes, including the experimental suggestion made by Touboul *et al.* [11]. The formation enthalpies of the energetically most stable structures have been taken from the OQMD database [35]. According to Figs. 2, 3, and 4, given the growth conditions-dependent formation energies, $TlVO_4$ could be synthesized exclusively using two competing binary compounds, namely V_2O_5 and Tl_2O_3. These binary oxides are taken as Tl_2O_3 with S.G. *Ia* $\overline{3}$ and V_2O_5 with S.G. *Pmn*21. The following restrictions are enforced to prevent the emergence of dual competing phases throughout the growth process:

$$\Delta H_{Tl_2O_3} > 2\Delta\mu_{Tl} + 3\Delta\mu_O \quad (4)$$

$$\Delta H_{V_2O_5} > 2\Delta\mu_V + 5\Delta\mu_O \quad (5)$$

In such ground conditions, we also have:

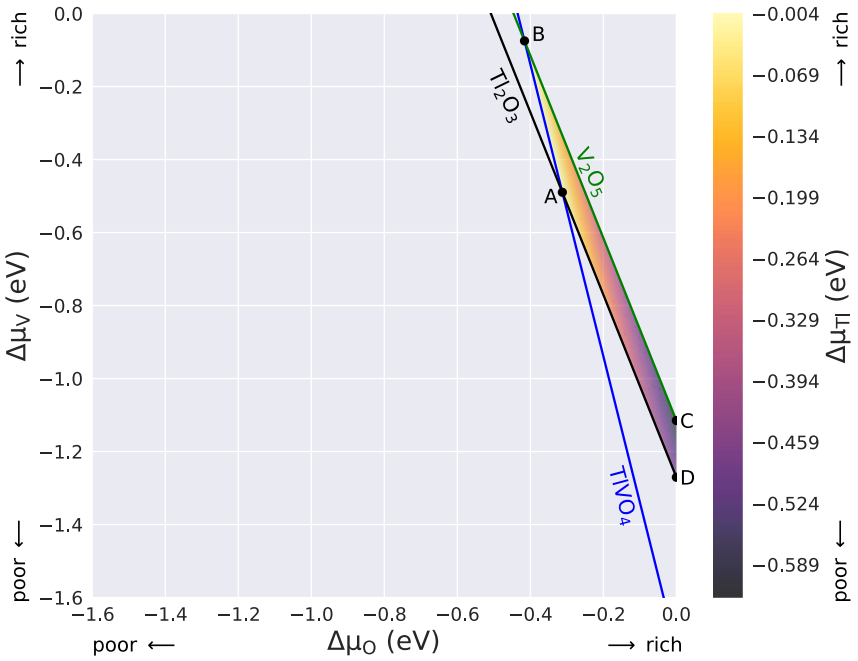

Fig. 2. (Color online) Calculated accessible range of chemical potentials for the equilibrium growth conditions of $TlVO_4$. We show the variation in $\Delta\mu_{Tl}$, as a function of $\Delta\mu_O$ and $\Delta\mu_V$ within the stability region. Color lines are the limits imposed by competing phases. A, B, C, D, and E delimit the stability area and represent the intersection points of conditions, see the Supl. Material [7].

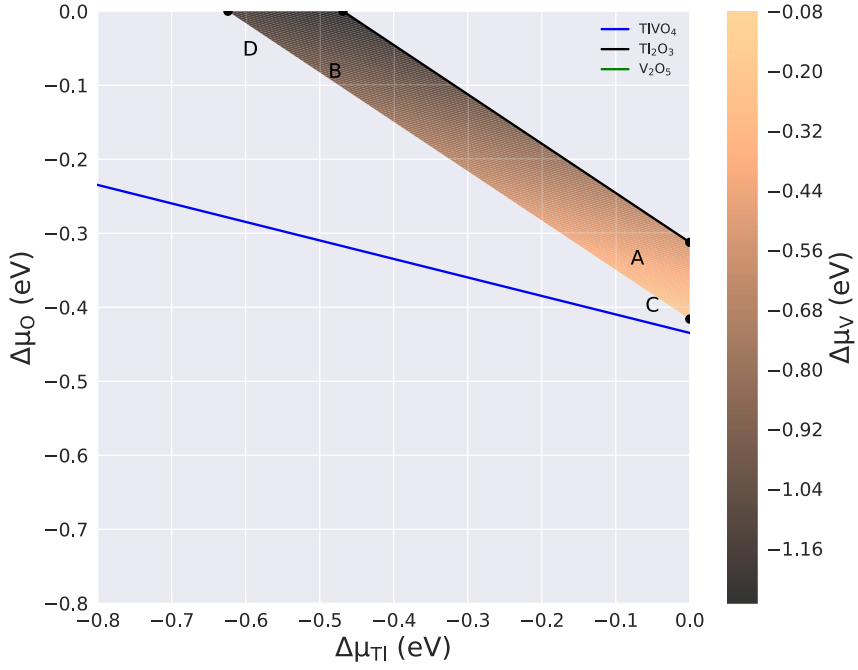

Fig. 3. (Color online) Calculated accessible range of chemical potentials for the equilibrium growth conditions of $TlVO_4$. We show the variation in $\Delta\mu_V$, as a function of $\Delta\mu_O$ and $\Delta\mu_{Tl}$ within the stability region. Color lines are the limits imposed by competing phases. A, B, C, D, and E delimit the stability area and represent the intersection points of conditions, see the Supl. Material [7].

$$\Delta\mu_{Tl} + \Delta\mu_V + 4\Delta\mu_O = \Delta\mu_{TlVO4} = -1.739\ eV \quad (6)$$

where Tl is a dependent variable:

$$(Tl_2O_3): -5\Delta\mu_O - 2\Delta\mu_V = 2.54\ eV \quad (7)$$

$$(V_2O_5): 5\Delta\mu_O + 2\Delta\mu_V = -2.23\ eV \quad (8)$$

where V is a dependent variable:

$$(Tl_2O_3): 2\Delta\mu_{Tl} + 3\Delta\mu_O = -0.93\ eV \quad (9)$$

$$(V_2O_5): -2\Delta\mu_{Tl} - 3\Delta\mu_O = 1.24\ eV \quad (10)$$

where O is a dependent variable:

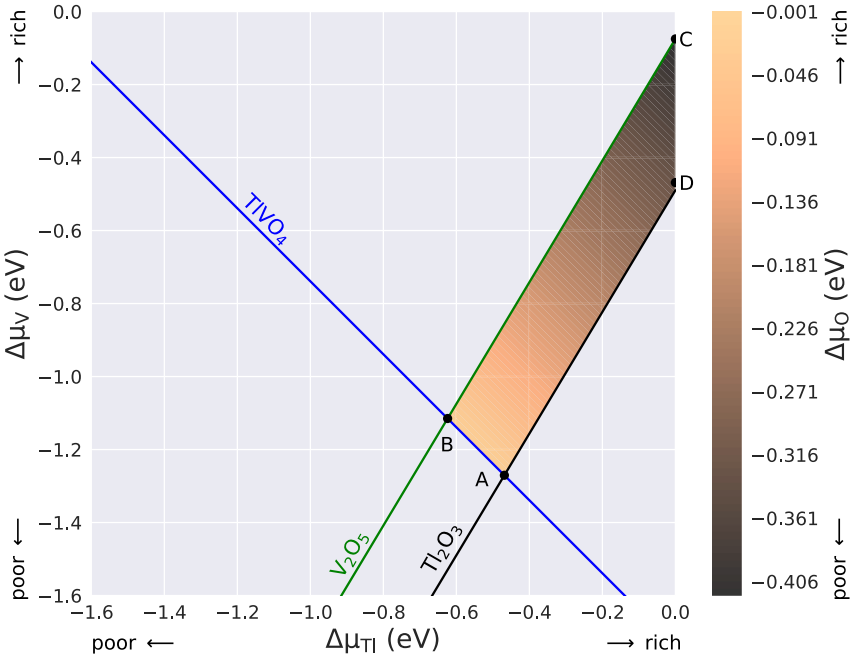

Fig. 4. (Color online) Calculated accessible range of chemical potentials for the equilibrium growth conditions of $TlVO_4$. We show the variation in $\Delta\mu_O$, as a function of $\Delta\mu_{Tl}$ and $\Delta\mu_V$ within the stability region. Color lines are the limits imposed by competing phases. A, B, C, D, and E delimit the stability area and represent the intersection points of conditions, see the Supl. Material [7].

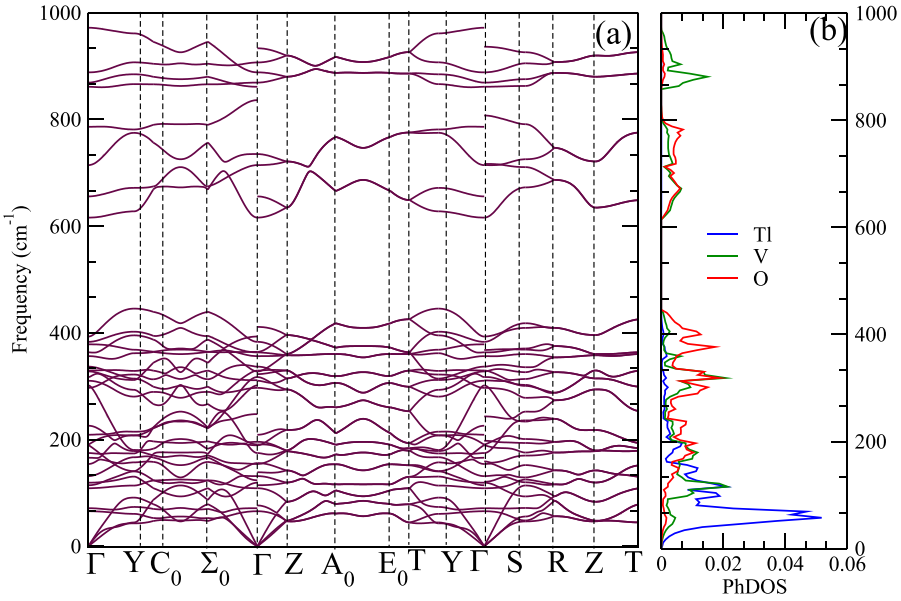

Fig. 5. (Color online) (a) Phonon dispersion of the stable orthorhombic structure of $TlVO_4$ at 0 GPa. (b) Partial phonon density of states (PhDOS) of the same structure. Both results are from AM05 calculations.

$$(Tl_2O_3) : 1.25\Delta\mu_{Tl} - 0.75\Delta\mu_V = 0.36\ eV \quad (11)$$

$$(V_2O_5) : -1.25\Delta\mu_{Tl} + 0.75\Delta\mu_V = -0.05eV \quad (12)$$

where μ_{Tl}, μ_V, and μ_O represent the chemical potentials of Tl, V, and O, respectively. The enthalpies $\Delta H(Tl_2O_3)$, and $\Delta E(V_2O_5)$ are equal to −0.937 and −2.23 eV, respectively. The larger area of stability in Fig. 4 determines that if the chemical potential of the oxygen atom is set as the dependent variable the growth of $TlVO_4$ is more favorable for the directional amount of the formation region (A-B) from V-poor and Tl-rich to Tl-rich and V-rich. Consequently the decomposition of $TlVO_4$ to $Tl_2O_3 + V_2O_5$ possible. This also means that the synthesis of $TlVO_4$ is favored by an oxidizing atmosphere.

To check both the dynamical and mechanical stability of the stable orthorhombic structure at 0 GPa, we have calculated the phonon dispersion as well as the elastic constants. The phonon dispersion (calculated with AM05) along the first Brillouin zone and the phonon density of states (DOS) are displayed in Fig. 5. The dispersion does not show any imaginary frequency, which is a proof of the dynamical stability of $TlVO_4$ in the orthorhombic structure. Since the crystal structure is composed of chains of edge-sharing TlO_6 octahedra linked by isolated VO_4 tetrahedra, which run parallel to the *c*-axis, (see Fig. S1 in

Table 2
Calculated wavenumbers (ω) of Raman, infrared, and silent modes using the PBE and AM05 functionals. The mode symmetry assignment is included. Results for IR modes extracted from previous experiments [37] are included for comparison.

Mode	PBE ω (cm^{-1})	Exp. ω (cm^{-1})	AM05 ω (cm^{-1})	Activity
A_u	65.7		65.7	silent
A_u	189.2		189.4	silent
A_u	383.7		383.7	silent
B_{3g}	107.0		108.9	Raman
A_g	133.4		131.6	Raman
B_{1g}	153.6		154.4	Raman
B_{1g}	175.2		174.9	Raman
B_{2g}	192.4		191.1	Raman
A_g	297.9		297.3	Raman
B_{3g}	317.6		317.5	Raman
B_{2g}	329.4		328.1	Raman
B_{1g}	338.6		337.1	Raman
A_g	357.4		356.8	Raman
B_{3g}	365.1		363.9	Raman
B_{1g}	616.1		616.9	Raman
A_g	713.6		715.4	Raman
B_{3g}	870.9		870.3	Raman
A_g	888.4		889.5	Raman
B_{1u}	71.1		71.4	IR
B_{3u}	116.3		114.5	IR
B_{1u}	118.9		119.3	IR
B_{2u}	155.9		156.1	IR
B_{2u}	196.6		196.0	IR
B_{3u}	208.8	235	209.3	IR
B_{1u}	301.6	275	301.8	IR
B_{3u}	311.8	300	310.6	IR
B_{2u}	329.4	328	329.7	IR
B_{2u}	366.5	378	393.7	IR
B_{1u}	392.6	415	364.8	IR
B_{3u}	654.4	680	656.6	IR
B_{2u}	735.2	730	736.1	IR
B_{1u}	862.2		862.5	IR
B_{2u}	909.5	890	908.1	IR

Supplementary Material [7]), the phonon modes of $TlVO_4$ at zero pressure can be classified as internal or external vibrations of the VO_4 units [36]. The calculated wavenumbers for zero pressure and temperature are summarized in Table 2. The two functionals give similar results.

According to the phonon DOS, the modes at wavenumbers larger than 800 cm^{-1} correspond to V-O vibrations, being associated with internal stretching vibrations of the VO_4 tetrahedron. In contrast, the modes in the 600–750 cm^{-1} region are associated with the vibration of V and Tl atoms. The phonon spectrum has a phonon gap between 415 and 600 cm^{-1} and the low-frequency vibrations have contributions from vibrations of O, V, and Tl atoms. According to the group theory analysis, at the Γ point of the Brillouin zone, the orthorhombic phase (S.G. *Cmcm*) obeys the following mechanical representation:

$$\Gamma = 5A_g + 4B_{1g} + 6B_{1u} + 3A_u + 2B_{2g} + 7B_{2u} + 4B_{3g} + 5B_{3u}.$$

One B_{1u}, one B_{2u} and one B_{3u} mode are the acoustic modes. In addition, there are three silent modes (A_u), fifteen infrared-active modes ($5B_{1u}$, $6B_{2u}$, and $4B_{3u}$), and fifteen Raman-active modes ($5A_g$, $4B_{1g}$, $2B_{2g}$, and $4B_{3g}$).

There is a previous IR experiment on $TlVO_4$ [37]. The wavenumbers of the previously reported modes are compared with our calculations in Table 2. The agreement is good. The maximum difference between calculated and measured modes is 30 cm^{-1}. This is for the B_{1u} mode with wavenumber 301.6/301.8 cm^{-1}, being the relative error 10%, which can be considered a very good agreement[38]. Our calculations provide, for the first time, a mode assignment for IR modes. In the previous experiments, the wavenumber cut-off of the setup was 200 cm^{-1}. Five of our calculated modes are below the cut-off, which explains why they were not measured. Above 200 cm^{-1} there is only one calculated mode not detected by the experiments. This is the B_{1u} mode with wavenumber 862 cm^{-1}. However, in experiments, the mode reported at 890 cm^{-1} is very broad and asymmetric. We believe this mode could be a doublet, including the two highest frequency modes we have calculated. Unfortunately, there are no Raman experiments to compare with and our calculations are provided to facilitate mode indentification in future Raman experiments. As a consequence, we will compare our calculated Raman modes with isostructural $InVO_4$ and $CrVO_4$. We have found that the distribution of Raman-active frequencies in $TlVO_4$ is qualitatively similar to that of $InVO_4$ and $CrVO_4$. In our compound, there are four modes between 600 and 890 cm^{-1}, and the other eleven modes are below the phonon gap. $InVO_4$ [5] ($CrVO_4$ [2]) has four high-frequency modes between 755 and 915 cm^{-1} (700 and 950 cm^{-1}) and the other eleven modes below the phonon gap. The resemblance of the high-frequency part of the Raman spectrum of the three vanadates is due to the similarity of the VO_4 tetrahedra.

To check the effect of the strain on the investigated compound, we have calculated the elastic constants within the stress method [22]. Single-crystal elastic constants under isotropic pressure of an orthorhombic structure should be assessed by means of the generalized Born criteria [29,39–43]. The calculated elastic constants for the orthorhombic structure are given in Table 3. Their values satisfy the mechanical stability conditions. Based on this and the eigenvalues calculated from the elastic constant matrix shown in Table S2 in the Supplementary Material [7], the orthorhombic structure of $TlVO_4$ is mechanically stable. From the table, we would like to highlight that the value of C_{11} is larger than the value of the C_{22} and C_{33} components. This result indicates that uniaxial compression can easily affect the *Cmcm* structure. By using the ELATE tool, we have extracted the bulk (K), Young (E), and shear (G) moduli within the Voigt (V) [44], Reuss (R) [45], and Hill (H) [46] approximations. The results corresponding to these moduli are presented in Table S3 in the Supplementary Material [7]. We can see that the calculated bulk modulus (56.8–66.3 GPa) from the elastic constants is in excellent agreement with the value estimated from the EOS fit of the energy versus volume results (See Table 1). In the S.M. [7], it can be seen that Young's modulus (64–69 GPa) is similar to the bulk modulus and that the shear modulus is much smaller (24.2–25.9 GPa). Thus, $TlVO_4$ has a greater resistance to unidirectional compression and volumetric compression than to shear deformation. This means that $CrVO_4$-type $TlVO_4$ is a soft material. In addition, the calculated Poisson's ratio, ~ 0.32, and B/G ratio, ~ 2.5 (see Table S3 in S.M. [7]), also indicate that the studied compound is a ductile material.

Table 3
Calculated elastic constants ($\mathbb{C}_{ij}$ in GPa) of $TlVO_4$ for the $CrVO_4$-type phase (*Cmcm*) at 0 GPa and the wolframite-type phase (*P2/c*) at selected pressures.

Phase	C_{11}	C_{12}	C_{13}	C_{15}	C_{22}	C_{23}	C_{25}	C_{33}	C_{35}	C_{44}	C_{46}	C_{55}	C_{66}
Cmcm (PBE)	152.08	48.44	56.76	–	76.14	32.56	–	102.23	–	19.49	–	21.88	24.26
Cmcm (AM05)	160.70	51.28	60.99	–	79.69	33.78	–	108.45	–	21.61	–	24.92	25.38
P2/c (PBE) at 3.1 GPa	227.41	102.37	120.45	– 2.95	153.50	93.97	– 18.23	226.19	– 7.02	37.32	– 16.92	56.19	2.51
P2/c (AM05) at 3.1 GPa	243.76	117.00	133.6	– 4.96	170.52	103.41	– 21.40	245.99	– 5.67	43.56	– 17.11	61.27	9.25
P2/c (PBE) at 13.6 GPa	267.83	147.57	161.25	– 9.99	185.27	123.91	– 33.34	261.80	– 5.84	40.90	– 17.69	57.92	20.73
P2/c (AM05) at 11.5 GPa	287.12	158.62	171.73	– 12.56	197.66	130.04	– 36.61	277.71	– 5.79	44.08	– 17.95	62.40	26.31

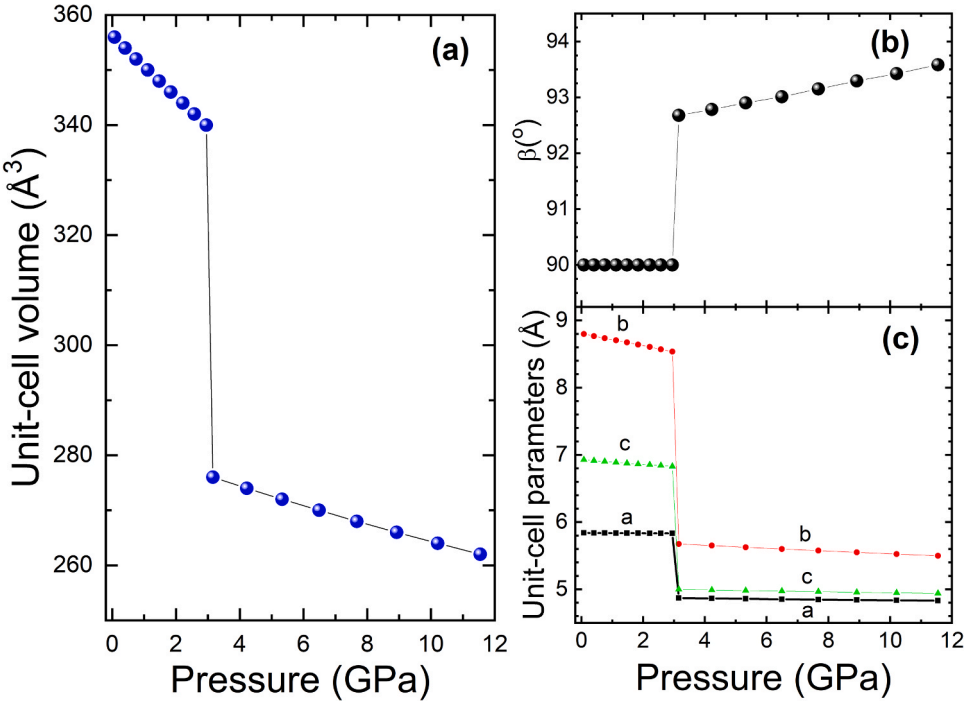

Fig. 6. (Color online) (a): Pressure dependence of the unit-cell volume of the ambient-pressure and high-pressure polymorphs of $TlVO_4$. The results have been calculated using AM05. For the HP phase, we plot 2*V* to facilitate the comparison. Notice that in the low-pressure phase Z = 4 and in the HP phase Z = 2. (b) Pressure dependence of the β angle and (c) pressure dependence of unit-cell parameters for the same structures.

3.2. *$TlVO_4$ under compression*

To explore the high-pressure structural stability of $TlVO_4$, twelve structures have been considered as candidates for a HP phase (see Computational details). They have been optimized for a number of sets of volumes. From these calculations, the enthalpy difference (ΔH) vs. pressure (P) plots have been extracted. They are shown in Fig. 1. This figure shows two structures that will have a lower enthalpy than the low-pressure phase under compression. The calculations predict a phase transition, at a relatively low pressure of ~ 2.7 GPa, from the orthorhombic $CrVO_4$-type structure (S.G. *Cmcm*) to a monoclinic wolframite-type phase described by S.G. *P2/c*. This HP phase remains thermodynamically the most favorable structure in the pressure range covered by this study. According to the enthalpy calculations, the fergusonite phase (S.G. *C2/c*) is in close competence with wolframite, however, its enthalpy is always slightly larger than that of wolframite. Thus according to thermodynamic arguments, the HP structural sequence of $TlVO_4$ is $CrVO_4$-type → wolframite-type. However, as we will explain in a subsequent paragraph, the wolframite-type structure is dynamically unstable beyond 6 GPa, which will have consequences in the HP behavior of $TlVO_4$. The structural information of the HP wolframite structure is summarized in Table 1 and Table S1 of the S. M. [7]. The crystal structure is schematically represented in Figure S1 of the S.M. [7]. The HP wolframite structure has two formula units in the unit cell. It consists of VO_6 irregular octahedra surrounding Tl atoms with an eight-fold coordination. The Tl coordination polyhedron is a square antiprism. This means that the phase transition involves the formation of new Tl-O bonds and V-O, increasing the coordination of Tl from six-fold to eight-fold and of V from four-fold to six-fold. This is a distinctive feature of $TlVO_4$ because in other $CrVO_4$-type vanadates only the coordination of vanadium is modified the HP phase transition occurs.

From the present DFT calculations, we have determined the pressure dependence of the unit-cell parameters and volume for the low- and high-pressure phases. The results are presented in Fig. 6. There it can be seen that there is an abrupt 18% volume decrease between the orthorhombic phase and HP phase. Such a volume collapse and the formation of additional bonds after the transition indicate that the phase transition is a first-order transformation. The observed increase in density of $TlVO_4$ is expected to make the material less compressible, after the phase transition. This phenomenon is mainly due to chemical bonding changes and the enhancement of the crystal packing, which induce the observed increase in the bulk modulus as shown in Table 1. The observed collapse of the volume is comparable to that reported for the pressure-induced $CrVO_4$-type to wolframite transition in $InVO_4$ (14%) and $CrVO_4$ (17%). However, in these two compounds, the transition involves only an increase in the coordination of V, which goes from four-fold to six-fold, and in the present case, as described in the previous paragraph, both the coordination of V and Tl are increased as a consequence of the phase transition. The differential behavior of $TlVO_4$ is due to the large ionic radii of Tl, which makes its coordination sphere quite sensitive to pressure. This fact is associated to the contribution to chemical bonding of Tl 6 s states. From the calculated unit-cell parameters, we obtained for the orthorhombic phase the linear compressibilities of each axis: $\kappa_a = 1.5 \times 10^{-3}$ GPa^{-3}, $\kappa_b = 8.5 \times 10^{-3}$ GPa^{-3}, and $\kappa_c = 3.6 \times 10^{-3}$ GPa^{-3}. This means that compression is anisotropic, being the *b*-axis the most compressible one (see Fig. 6). In this regard, the behavior is similar to the non-isotropic behavior of $CrVO_4$ and $InVO_4$. For the high-pressure phase, the behavior is also non-isotropic. In this case, since the structure is monoclinic, and "*a*", "*b*", "*c*", and the β angle change with pressure (see Fig. 6), the main axes of compressibility and the associated compressibility should be determined to describe the change of the crystal structure. We obtained $\kappa_1 = 3.9 \times 10^{-3}$ GPa^{-3}, $\kappa_2 = 2.3 \times 10^{-3}$ GPa^{-3}, and $\kappa_3 = 1.7 \times 10^{-3}$ GPa^{-3}. The corresponding axes of compressibility are (010), (304), and (40$\bar{3}$). As in the low-pressure phase the most compressible direction corresponds to the *b*-axis.

In order to further check the stability of the wolframite-type phases, we have studied its dynamical stability by calculating the phonon dispersion at pressures where it has been predicted to be the lowest-enthalpy phase. As we will show, this criterion is not satisfied by the wolframite-type structure beyond 6 GPa. We have also found that the fergusonite structure, the closest phase in enthalpy to wolframite after the phase transition, is dynamically unstable. We have also explored the

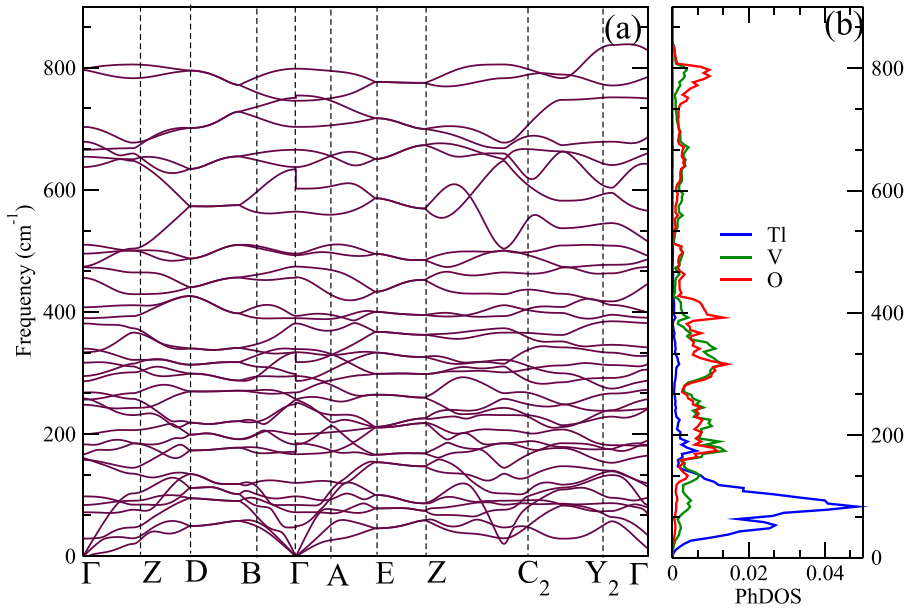

Fig. 7. (Color online) (a) Phonon dispersion of the HP monoclinic *P2/c* structure of $TlVO_4$ at 3.1 GPa. (b) Partial phonon density of states (PhDOS) of the same structure. Both results are from AM05 calculations.

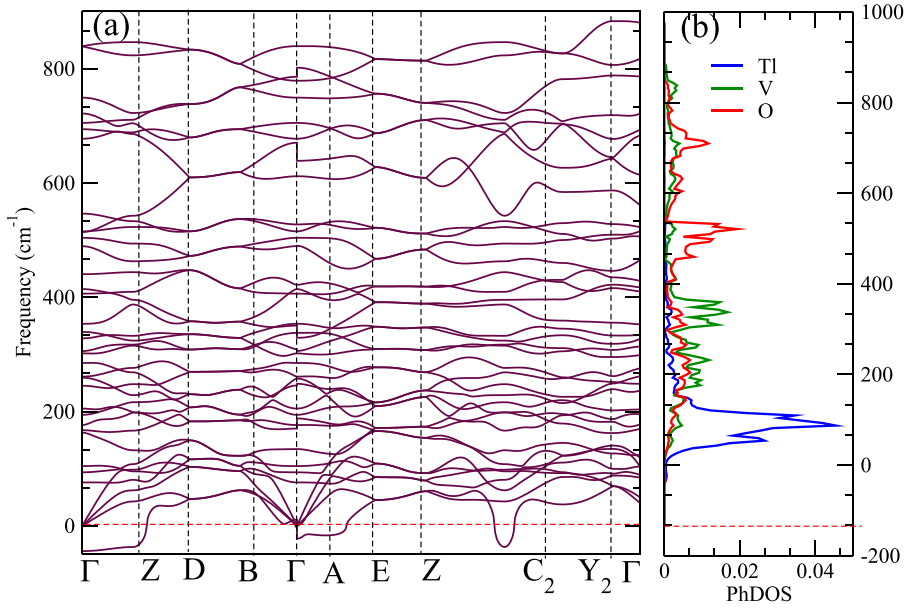

Fig. 8. (Color online) (a) Phonon dispersion plot of the P2/c phase at 11.5 GPa showing imaginary modes (b) Partial phonon density of states (PhDOS) of the same structure. Both results are from AM05 calculations.

mechanical stability by calculating the elastic constants as a function of pressure. The mechanical stability of the wolframite phase is fulfilled. This can be seen in Table S2 of the Supplementary Material [7]. The calculated phonon dispersion of the wolframite structure at 3.1 GPa is shown in Fig. 7. All phonon branches are positive supporting the dynamical stability of wolframite after the phase transition. However, at a pressure of 6 GPa and higher, we have found that dynamical instabilities develop in the wolframite structure. This can be seen in Fig. 8 where it can be seen that there is a phonon branch that becomes imaginary. The mode that softens under compression is the acoustic B_{1u} branch which becomes negative in several points of the Brillouin zone, as shown in Fig. 8. More information on the pressure dependence of this and the rest of the modes can be found in Figures S2 and S3 in the SM file [7]. Additionally, the fergusonite phase is dynamically unstable at all pressures, meaning that a transition from wolframite to fergusonite is not possible. This can be seen in the phonon dispersion represented in Figure S4 in the SM file [7], which shows that at 3.2 GPa there is a phonon branch that is negative near the *A* point of the Brillouin zone. Thus, we can conclude that both the wolframite and fergusonite phases are unstable beyond 6 GPa.

The above-described results lead us to consider alternative scenarios. We simulate the decomposition of $TlVO_4$ into $TlVO_3 + 1/2\ O_2$ and $Tl_2O_3 + V_2O_5$. The comparison of the enthalpies of $TlVO_4$ and its daughter products is shown in Figs. 9 and 10. At the same time, we can notice that the conditions for decomposition for daughter binary compounds diminish making it unfavorable (see Figures S5, S6, and S7 of the S.M. [7]). In the figures, it can be seen that the decomposition product has a higher enthalpy than the low-pressure phase of $TlVO_4$ and therefore also

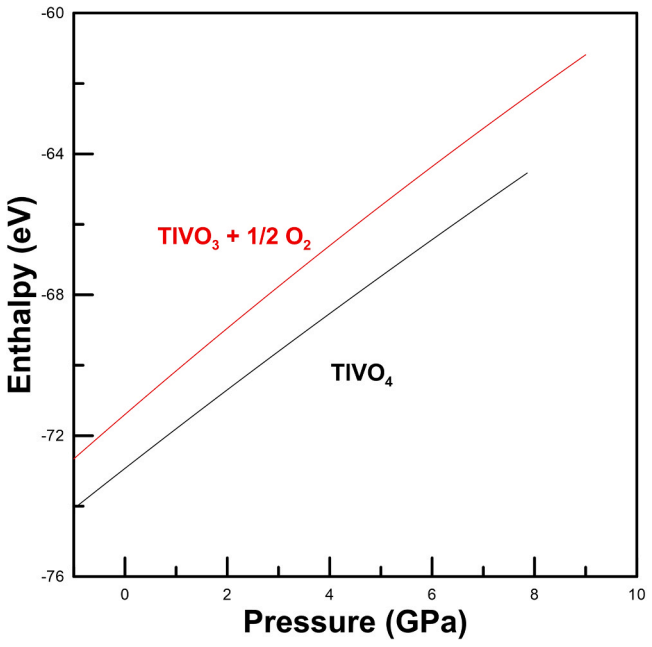

Fig. 9. (Color online) Calculated enthalpy versus pressure for the low-pressure phase of $TlVO_4$ and its decomposition products ($TlVO_3$ + 1/2 O_2). Here the enthalpy of $TlVO_4$ and ($TlVO_3$ + 1/2 O_2) is represented respectively by black, and red lines.

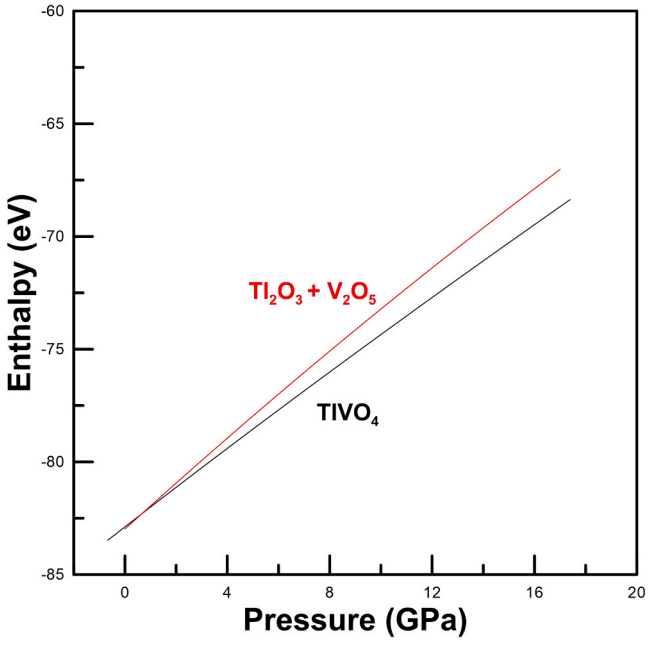

Fig. 10. (Color online) Calculated enthalpy versus pressure for the decomposition (Tl_2O_3 + V_2O_5). Here the enthalpy of $TlVO_4$ and (Tl_2O_3 + V_2O_5) is represented respectively by black and red lines.

than any structure with a lower enthalpy, such as the HP polymorph. Our results show that pressure, in contrast to temperature, which favors the decomposition of $TlVO_4$, inhibits the decomposition of $TlVO_4$ making the difference of enthalpy between $TlVO_4$ and its daughter products larger as pressure is increased. Therefore, we hypothesize that the dynamical instabilities driven by pressure beyond 6 GPa might be due to a pressure-driven amorphization, which would cause a loss of long-range order in crystalline $TlVO_4$ disrupting the regular arrangement of its atoms [47]. One of the possible causes of amorphization is

Table 4
Calculated A_g, B_g, A_u, and B_u phonon modes for the *P*2/*c* phase at 3.1 GPa using the AM05 functional. IR and R identify the infrared and Raman modes, respectively.

B_u(IR)	31.0
A_u(IR)	120.7
B_u(IR)	159.6
B_u(IR)	249.9
A_u(IR)	258.4
B_u(IR)	290.4
B_u(IR)	318.2
A_u(IR)	338.9
A_u(IR)	397.1
B_u(IR)	457.2
B_u(IR)	475.8
A_u(IR)	493.4
A_u(IR)	563.9
B_u(IR)	678.9
A_u(IR)	748.0
B_g(R)	72.8
A_g(R)	83.5
B_g(R)	98.1
B_g(R)	168.5
B_g(R)	186.9
A_g(R)	201.0
B_g(R)	257.2
A_g(R)	270.0
A_g(R)	294.2
B_g(R)	336.3
B_g(R)	383.5
A_g(R)	390.6
B_g(R)	476.3
A_g(R)	498.1
B_g(R)	638.8
A_g(R)	666.5
B_g(R)	704.1
A_g(R)	795.6

the strong preference of the crystal structures for shear stress. This hypothesis is consistent with the fact that the mechanical instability detected from the elastic tensor is driven by the decrease of the C_{44} and C_{55} constants, a phenomenon known as shear-mode softening, which has been connected to pressure-driven amorphization [48]. Pressure-induced amorphization has not been observed before in other orthovanadates. Interestingly, pressure-induced amorphization has been reported for Tl_2O_3, but not for Cr_2O_3 and In_2O_3, suggesting that amorphization could be a distinctive feature of binary and ternary thallium oxides. An additional possible fact beyond it, it could be a pressure-driven delocalization of 4 f electrons of Tl atoms. The computing simulation of amorphous $TlVO_4$ is beyond the scope of this study. We would like to stress here that amorphization of $TlVO_4$ at 6 GPa is an unprecedented phenomenon at such low pressures in orthovandates and related oxides which deserves to be further study to understand this phenomenon and its implications for industrial applications of $CrVO_4$-type vanadates.

To complete the discussion of this section, we will discuss the Raman and IR spectra of the HP wolframite-type phase of $TlVO_4$. According to the group theory analysis, at the Γ point of the Brillouin zone, the wolframite phase (S.G. *P*2/*c*) follows the flowing mechanical representation:

$$\Gamma = 8A_g + 10B_g + 8A_u + 10B_u$$

Two B_u and A_u modes are the acoustic modes. In addition, there are fifteen infrared-active modes ($7A_u$ and $8B_u$), and eighteen Raman-active modes ($8A_g$ and $10B_g$). The calculated wavenumbers of the modes of the HP phase at 3.1 GPa are reported in Table 4. Regarding the atomic contribution to vibrations, in Fig. 7, it can be seen that high-frequency phonons are associated with vibrations of oxygen atoms. Indeed, they are internal stretching vibrations of the VO_6 octahedron. It can also be

Table 5
Topological charges and volumes of polymorphic sequences at their pressure transitions. Note that even though the *P2/c* (Z = 2) structure represents the HP phase, the atomic volume of Tl in this phase is higher than that of Tl in the ground structure *Cmcm* (Z = 4). The volume of Tl increases because of the rise of the Tl coordination number from 6 to 8.

phase	atom	Volume (bohr^3)	atomic charge
Cmcm	Tl	53.114	2.39
	V	31.286	2.00
	O	51.292	− 1.19
	O	64.472	− 1.12
	O	45.545	− 0.87
	O	51.296	− 1.19
P2/c	Tl	88.301	1.76
	V	29.128	2.62
	O	77.519	−1.06
	O	73.937	−1.13

noted that, in contrast to the low-pressure phase, in wolframite the phonon gap is from 490 to 560 cm^{-1}. The modes below 490 cm^{-1} have contributions from all atoms, being associated with bending vibrations of the VO_6 octaahedron, and to vibrations of Tl atoms and VO_6 octahedra as rigid units.

From calculations, we have also obtained the pressure dependence of phonons, which is plotted in Figure S3 of the S.M. [7]. This information is provided to facilitate comparison with future experiments. The pressure dependence of the phonons shows two interesting features. In the low-pressure phase, there are two phonons that soften under compression. The Raman mode B_{1g} and the IR mode B_{3u}. The existence of such modes is usually related to the occurrence of a phase transition [49] as we found near 3 GPa. In the high-pressure phase, there is also a mode slightly softening under compression, the lowest frequency B_g mode, and an IR B_u mode which softens becoming the frequency zero beyond 6 GPa, as happens with one of the acoustic modes. In addition, there are modes that tend to merge as pressure increases (see Figure S3 of the S.M. [7]). The mode softening observed in wolframite is consistent with the fact that the HP structure becomes dynamically unstable beyond 6 GPa, as we discussed before.

3.3. Changes in bonding and electronic properties along the Cmcm ⟶ P2/c phase transition

When atoms are compressed in the solid state, they are subjected to an additional confinement potential. The "chemical bonding" is therefore very different from that at ambient conditions. Thus, it is necessary to analyze pressure-induced changes in bonding. Hopefully, enormous developments in analyzing the behavior of the wave function have taken place in the last few years. They allow us to analyze the bonding path along the pressure-driven phase transition in $TlVO_4$. To achieve this goal, we have made a topological analysis of the charge density of the stable phases and extracted volumes and topological charges. The results are displayed in Table 5. We have found that along the pressure-induced polymorphic sequence, *Cmcm* ⟶ *P2/c*, there is a decrease of the charge transfer from Tl and V to O atoms. This is because pressure plays the role of equalizing both the negative charges of the non-equivalent oxygen atoms and the positive charges of the two cations. Thus, whereas the *Cmcm* phase shows three clearly different oxygen atoms with charges of −1.2, −1.1, and −0.87 and two different cations ($Tl^{+2.4}$ and V^{+2}.), in the *P2/c* phase, oxygen charges are very similar (− 1.06 and − 1.13), and the opposite occurs in the cations ($Tl^{+1.76}$ y $V^{+2.62}$). The relative positions of the cations and anions in both structures explain the differences in the charges. The oxygen atoms which are the nearest neighbors of cations are the atoms with the most negative charge. As we move from the low- to the high-pressure phase, cation-oxygen and oxygen-oxygen distances increase as a consequence of the modifications of coordination polyhedra. As a result, the anisotropy of the local atomic environment decreases. This is one of the reasons for stabilizing the high-pressure phase. It has been also found that the compression of the $TlVO_4$ cell affects the distances between atoms and alters the overlap of electron orbitals, leading to changes in the energy levels of the valence and conduction bands.

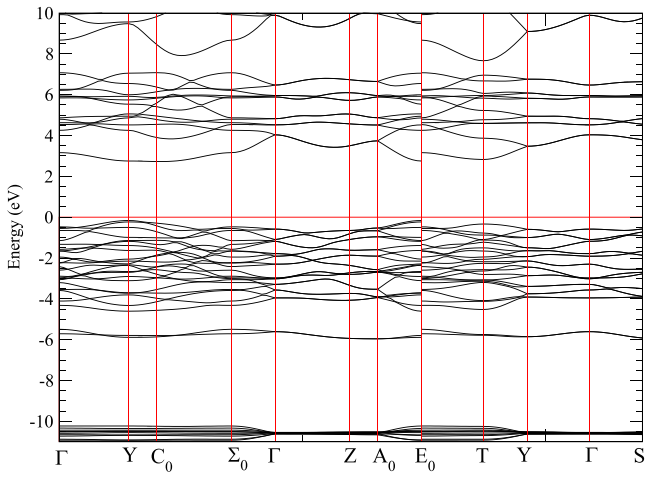

Fig. 11. (Color online) Electronics band structure of the $CrVO_4$-type phase calculated at 0 GPa using the HSE06 functional.

Table 6
Band-gap energy of the two phases of $TlVO_4$ calculated using the HSE06 functional.

phase	E_g	experiment
Cmcm at 0 GPa	2.89	2.94[a]
P2/c at 3.1 GPa	3.13	

[a] Ref. [12]

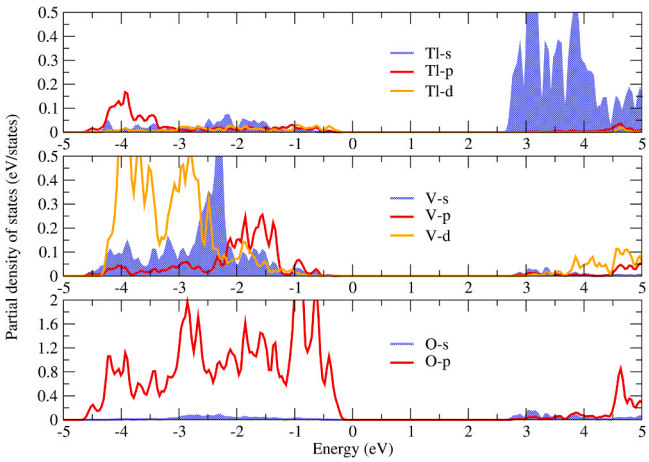

Fig. 12. (Color online) Calculated projected electronic density of states of the *Cmcm* phase at 0 GPa.

Let discuss now the band structure and electronic density of states. We display in Fig. 11 the electronic band structure of the *Cmcm* phase at zero pressure. The band structure has been calculated using the HSE06 functional, which is known to give more accurate values of the band-gap energy than PBE and AM05 [50], $CrVO_4$-type $TlVO_4$ has a direct band gap at the Y-Y point of the Brillouin zone with a value of 2.89 eV. The calculated band gap agrees within uncertainties with the experimental band gap of 2.94(5) eV determined from photoluminescence measurements [12] (see Table 6). Our calculations indicate that the top of the valence band is dominated by O 2*p* and V 3*p* states and the bottom of the

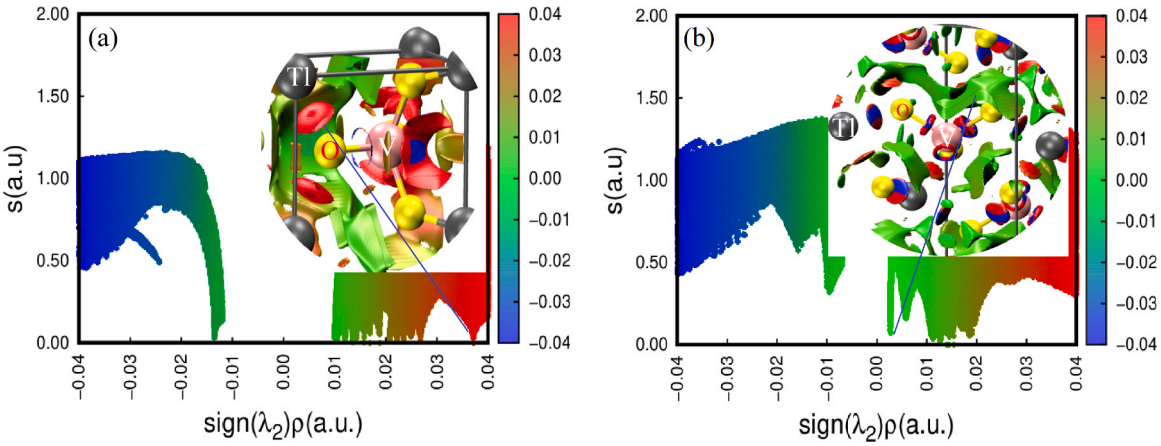

Fig. 13. (Color online) Reduced density gradient $S(\mathbf{r})$ vs $sign(\lambda_2)\rho(\mathbf{r})$ for both structure, *Cmcm* at 0 GPa and *P*2/*c* at 3.1 GPa. The insets give the corresponding 3D NCI isosurface at $S(\mathbf{r}) = 0.3$.

conduction band by Tl 6*s* states; see Fig. 12. This is a distinctive feature because in orthovanadate compounds usually the states near the Fermi level are dominated by O and V orbitals. The change in the crystal structure at the phase transition led to an increase in the band-gap energy which is equal to 3.13 eV at 3.1 GPa. This increase of the band-gap energy is different from the decrease of the band-gap energy at the $CrVO_4$-to-wolframite transition in $InVO_4$ and $CrVO_4$ [2,5]. The HP phase has a direct and an indirect band gap with the same energy, having two degenerated minima in the conduction band at a C_O and E_O points of the Brillouin zone and two degenerated maxima in the valence band located at the *Y* and E_0 points (see Figure S8 in the S.M. [7]). This change in the band-structure topology is mainly due to the difference in atomic spacing between the low- and high-pressure structures that modify the electrostatic forces acting on the electrons, thus altering their energy states. In the HP phase the top of the valence band is dominated only by O 2*p* states and the minimum of the conduction band by Tl 6*s* with a minor contribution of O 2*s* states (see Figure S9 in the S.M. [7]). The change of the orbital contribution to states near the Fermi level is what favors the increase of the band-gap energy at the phase transition. The 3.1 eV band gap of the wolframite phase and the potential fact that it can be possibly synthesized as a metastable phase could have important implications for applications of $TlVO_4$. In particular, a band gap of 3.1 eV makes wolframite-type $TlVO_4$ more suitable for the photocatalytic treatment of residual dyes from different sources and a wide variety of organic pollutants introduced into the natural water resources.

To gain a deeper insight into the new electronic configuration, we have also analyzed the bonding changes through the NCI plot derived from quantum-mechanical calculations [27,51]. This tool can provide insights into the strength and nature of intermolecular interactions. This index visualizes electronic domains indexed by color gradient, which quantifies the strength of non-covalent interactions at each point in space through the reduced density gradient RDG or $S(\mathbf{r})$ map [52]. It uses the sign of the second-largest eigenvalue of the Hessian matrix at each isosurface point. In this way, we could distinguish between supposedly attractive ($sign(\lambda_2)\rho(\mathbf{r}) < 0$), allegedly repulsive ($sign(\lambda_2)\rho(\mathbf{r}) > 0$) and finally, the van der Waals ($sign(\lambda_2)\rho(\mathbf{r}) \simeq 0$) interactions. $S(\mathbf{r})$ versus $sign(\lambda_2)\rho(\mathbf{r})$ plots for both *Cmcm* and *P*2/*c* HP structures are displayed in Figs 13(a) and (b). We can show that both structures contain regions where the non-covalent interactions are relatively weak or insignificant. The transition from *Cmcm* to *P*2/*c* phase induces a decrease in repulsive interactions in red. This can be seen near $sign(\lambda_2)\rho(\mathbf{r}) \sim 0.04$ of Fig. 13(a). The transition is also characterized by a change in the nature of the disc-shaped region located between Tl and O atoms. The isosurface around the Tl–O bond becomes darker, indicating stronger interactions, mainly due to the increase in ionicity in the unit cell. Interestingly, there is a strong overlap of electronic clouds in the VO_6 unit, which occurs in close proximity to the V–O bonds, the signature of steric hindrance; this trend is rather due to the enhancement of repulsion in the wolframite-type phase.

4. Conclusions

We have presented a systematic density-functional theory study of the high-pressure behavior of $TlVO_4$. We have described the structural, vibrational, elastic, and electronic properties of $TlVO_4$ at ambient conditions and under high pressure, We have also found that $TlVO_4$ undergoes a phase transition at 2.7 GPa to a monoclinic structure. The structural transition involves an increase in the coordination number of thallium and vanadium atoms. The phase transition also induces a change in the band-gap energy, which has been explained by changes induced in bonding. Upon further compression, $TlVO_4$ has been proposed to undergo pressure-driven amorphization at 6 GPa, a fact never observed before in orthovanadates at such low pressures. Decomposition of $TlVO_4$ has been also found to be not possible, The distinctive behavior of $TlVO_4$ under compression seems to be related to the contribution of Tl 6*s* states to bonding. The reported results are the missing piece to the puzzle of the behavior of orthovanadates under high pressure.

CRediT authorship contribution statement

Tarik Ouahrani: Writing – review & editing, Writing – original draft, Validation, Investigation, Formal analysis. **A. Muñoz:** Writing – review & editing, Writing – original draft, Validation, Methodology, Investigation. **Ruth Franco:** Writing – review & editing, Investigation. **Z. Bedrane:** Writing – review & editing, Investigation. **R. M. Boufatah:** Writing – review & editing, Investigation. **Daniel Errandonea:** Writing – review & editing, Writing – original draft, Supervision, Project administration, Methodology, Investigation, Formal analysis, Conceptualization.

Declaration of Competing Interest

The authors declare that they have no known competing financial interests or personal relationships that could have appeared to influence the work reported in this paper.

Data Availability

Data will be made available on request.

Acknowledgments

T.O. thanks the financial support obtained through PRFU B00L02EP130220230001. D.E. and A.M. thanks the financial support of the Spanish Ministry of Science and Innovation (MCIN/AEI/10.13039/501100011033) under grants number PID2019-106383GB-C41/43, PID2022-138076NB-C41/44, and RED2022-134388-T. D.E. thanks the support from the Generalitat Valenciana (GV) under grants CIPROM/2021/075 and MFA/2022/007. This study is part of the Advanced Materials program supported by MCIN and GV with funding from the European Union NextGenerationEU (PRTR-C17. I1). R.F. thanks the financial support from the Spanish National Research Agency (AEI) through project PID2021–122588-NB-C21. D.E. thanks the Tirant supercomputer (Univ. de Valencia) for providing computational resources.

Appendix A. Supporting information

Supplementary data associated with this article can be found in the online version at doi:10.1016/j.jallcom.2024.173483.

References

[1] D. Errandonea, High-pressure crystal structures of orthovanadates and their properties, J. Appl. Phys. 128 (2020) 040903.
[2] P. Botella, S. López-Moreno, D. Errandonea, F.J. Manjón, J.A. Sans, D. Vie, A. Vomiero, High-pressure characterization of multifunctional $CrVO_4$, J. Phys.: Condens. Matter 32 (2020) 385403.
[3] E.J. Baran, Materials belonging to the $CrVO_4$ structure type: preparation, crystal chemistry, and physicochemical properties, J. Mater. Sci. 333 (1998) 2479–2497.
[4] S. López-Moreno, D. Errandonea, Ab initio prediction of pressure-induced structural phase transitions of $CrVO_4$ -type orthophosphates, Phys. Rev. B 86 (2012) 104112.
[5] D. Errandonea, Oscar Gomis, B. García-Domene, J. Pellicer-Porres, V. Katari, S. NagabhusanAchary, A.K. Tyagi, C. Popescu, New polymorph of InVO4 a high-pressure structure with six-coordinated vanadium, Inorg. Chem. 52 (2013) 12790–12798.
[6] J. Gonzalez-Platas, S. Lopez-Moreno, E. Bandiello, M. Bettinelli, D. Errandonea, Precise characterization of the rich structural landscape induced by pressure in multifunctional $FeVO_4$, Inorg. Chem. 59 (2020) 6623–6630.
[7] See electronic Supplemental Material for additional information.2023.
[8] S. López-Moreno, P. Rodríguez-Hernández, A. Muñoz, D. Errandonea, First-principles study of $InVO_4$ under pressure: phase transitions from $CrVO_4$ - to $AgMnO_4$ -type structure, Inorg. Chem. 56 (5) (2017) 2697–2711.
[9] P.B. Romero-Vázquez, S. López-Moreno, D. Errandonea, Stability of $FeVO_4$ -II under pressure: a first-principles study, Crystals 12 (2022) 1835.
[10] M. Touboul, P. Toledano, Structure du vanadate d'indium: $InVO_4$, Acta Cryst. B36 (1980) 240–245.
[11] M. Touboul, D. Ingrain, Synthéses et propriétés thermiques de $InVO_4$ et $TlVO_4$, J. Less-Common Met. 71 (1980) 55–62.
[12] D.P. Butcher Jr., A.A. Gewirth, Photoelectrochemical response of $TlVO_4$ and $InVO_4$: $TlVO_4$ composite, Chem. Mater. 22 (2010) 2555–2562.
[13] V. Panchal, F.J. Manójn, D. Errandonea, P. Rodriguez-Hernandez, J. López-Solano, A. Muñoz, N. Achary, A.K. Tyagi, High-pressure study of $ScVO_4$ by Raman scattering and ab initio calculations, Phys. Rev. B 83 (2011) 064111.
[14] G. Kresse, J. Furthmüller, Efficiency of ab-initio total energy calculations for metals and semiconductors using a plane-wave basis set, Comput. Mat. Sci. 6 (1996) 15.
[15] G. Kresse, J. Hafner, Ab initio molecular dynamics for liquid metals, Phys. Rev. B 47 (1993) 558–561.
[16] H.Z. Guedda, T. Ouahrani, A. Morales-García, R. Franco, M.A. Salvadó, P. Pertierra, J.M. Recio, Computer simulations of 3C-SiC under hydrostatic and non-hydrostatic stresses, Phys. Chem. Chem. Phys. 18 (2016) 8132.
[17] P.E. Blochl, Projector augmented-wave method, Phys. Rev. B 50 (1994) 17953.
[18] J.P. Perdew, K. Burke, M. Ernzerhof, Generalized gradient approximation made simple, Phys. Rev. Lett. 77 (1996) 3865.
[19] J.P. Perdew, A. Ruzsinszky, G.I. Csonka, O.A. Vydrov, G.E. Scuseria, L. A. Constantin, X. Zhou, K. Burke, Restoring the density-gradient expansion for exchange in solids and surfaces, Phys. Rev. Lett. 100 (2008) 136406.
[20] A.E. Mattsson, R. Armiento, The subsystem functional scheme: the Armiento-Mattsson 2005 (AM05) functional and beyond, Spec. Issue.: Proc. 13th Ed. Int. Conf. Appl. Density Funct. Theory Chem. Phys. 110 (2010) 2274–2282.
[21] H.J. Monkhorst, J.D. Pack, Special points for Brillouin-zone integrations, Phys. Rev. B 13 (1976) 5188.
[22] O.H. Nielsen, R.M. Martin, Quantum-mechanical theory of stress and force, Phys. Rev. B 32 (1985) 3780–3791.
[23] A. Togo, I. Tanaka, First principles phonon calculations in materials science, Scr. Mater. 108 (2015) 1–5.
[24] X. Gonze, C. Lee, Dynamical matrices, Born effective charges, dielectric permittivity tensors, and interatomic force constants from density-functional perturbation theory, Phys. Rev. B 55 (1997) 10355–10368.
[25] A. Otero-de-la-Roza, M.A. Blanco, A. MartínPendás, V. Luaña, Critic: a new program for the topological analysis of solid-state electron densities, Comput. Phys. Commun. 180 (2009) 157–166.
[26] RFW Bader, Atoms in Molecules, Oxford University Press, Oxford, 1990.
[27] S. Belarouci, T. Ouahrani, N. Benabdallah, A. Morales-García, I. Belabbas, Two-dimensional silicon carbide structure under uniaxial strains, electronic and bonding analysis, Comp. Mater. Sci. 151 (2018) 288–295.
[28] T. Ouahrani, R. Khenata, B. Lasri, A.H. Reshak, A. Bouhemadou, S. Bin-Omran, First and second harmonic generation of the XAl_2Se_4 (X= Zn, Cd, Hg) defect chalcopyrite compounds, Phys. B: Condens. Matter 407 (18) (2012) 3760–3766.
[29] S. Belarouci, T. Ouahrani, N. Benabdallah, A. Morales-García, R. Franco, Quantum-mechanical simulations of pressure effects on $MgIn_2S_4$ polymorphs, Phase Transit 91 (2018) 759–771.
[30] J. Buckeridge, D.O. Scanlon, A. Walsh, C.R.A. Catlow, Automated procedure to determine the thermodynamic stability of a material and the range of chemical potentials necessary for its formation relative to competing phases and compounds, Comput. Phys. Commun. 185 (2014) 330–338.
[31] R.M. Boufatah, T. Ouahrani, M. Benaissa, Electronic and optical properties of wolframite-type ScNbO4: the effect of the rare-earth doping, Eur. Phys. J. B 95 (2022) 166.
[32] D. Errandonea, F.J. Manjon, Pressure effects on the structural and electronic properties of ABX_4 scintillating crystals, Prog. Mat. Sci. 53 (2008) 711–773.
[33] F. Birch, Finite elastic strain of cubic, Phys. Rev. 71 (1947) 809–824.
[34] D. Errandonea, A.B. Garg, Recent progress on the characterization of the high-pressure behavior of AVO_4 orthovanadates, Prog. Mat. Sci. 97 (2018) 123–169.
[35] S. Kirklin, J.E. Saal, B. Meredig, A. Thompson, J.W. Doak, M. Aykol, S. Rühl, C. Wolverton, The Open Quantum Materials Database (OQMD): assessing the accuracy of DFT formation energies, npj Comput. Mater. 1 (2015) 15010.
[36] T. Marqueño, J. Pellicer-Porres, D. Errandonea, D. Santamaria-Perez, D. Martinez-Garcia, P. Rodríguez-Hernández, A. Muñoz, I. Nieves-Pérez, S.N. Achary, M. Bettinelli, Lattice dynamics of zircon-type $NdVO_4$ and scheelite-type $PrVO_4$ under high-pressure, J. Phys.: Condens. Matter 34 (2022) 025404.
[37] E.J. Baran, M.E. Escobar, The vibrational spectra of $InVO_4$ and $TlVO_4$, Spectrochim. Acta 41 (1985) 415–417.
[38] D. Errandonea, A. Muñoz, P. Rodríguez-Hernández, O. Gomis, S.N. Achary, C. Popescu, S.J. Patwe, A.K. Tyagi, High-pressure crystal structure, lattice vibrations, and band structure of $BiSbO_4$, Inorg. Chem. 55 (2016) 4958–4969.
[39] L. Gerward, J.S. Olsen, L. Petit, G. Vaitheeswaran, V. Kanchana, A. Svane, Bulk modulus of CeO_2 and PrO_2 -an experimental and theoretical study, J. Alloy Compd. 400 (2005) 56–61.
[40] T. Gurel, R. Eryigit, Ab initio pressure-dependent vibrational and dielectric properties of CeO_2, Phys. Rev. B 74 (2006) 014302.
[41] T. Ouahrani, F.-Z. Medjdoub, S. Gueddida, Á. Lobato Fernandez, R. Franco, N.-E. Benkhettou, M. Badawi, A. Liang, J. Gonzalez, D. Errandonea, Understanding the pressure effect on the elastic, electronic, vibrational, and bonding properties of the $CeScO_3$ perovskite, J. Phys. Chem. C 125 (1) (2021) 107–119.
[42] G. Grimvall, B. Magyari-Köpe, V. Ozoliņš, K.A. Persson, Lattice instabilities in metallic elements, Rev. Mod. Phys. 84 (2012) 945.
[43] L. Gerward, J.S. Olsen, Powder diffraction analysis of cerium dioxide at high pressure, Powder Diffr. 8 (1993) 127–129.
[44] W. Voigt, ed. Teubner, 1928, Leipzig.
[45] A. Reuss, Berechnung der Fließgrenze von Mischkristallen auf Grund der Plastizitätsbedingung für Einkristalle, Z. Angew. Math. Mech. 9 (1929) 49–58.
[46] R. Hill, The elastic behaviour of a crystalline aggregate, Proc. Phys. Soc. A 65 (1952) 349.
[47] J. Singh, S.S. Sahoo, K. Venkatakrishnan, G. Vaitheeswaran, D. Errandonea, High-pressure study of the aurophilic topological Dirac material AuI, J. Alloy Compd. 928 (2022) 167178.
[48] A.U. Ortiz, A. Boutin, A.H. Fuchs, F.X. Coudert, Investigating the pressure-induced amorphization of zeolitic imidazolate framework ZIF-8: mechanical instability due to shear mode softening, J. Phys. Chem. Let. 4 (2013) 1861–1865.
[49] A. Liang, S. Rahman, P. Rodriguez-Hernandez, A. Munoz, F.J. Manjon, G. Nenert, D. Errandonea, High-pressure Raman study of $Fe(IO_3)_3$: soft-mode behavior driven by coordination changes of iodine atoms, J. Phys. Chem. C 124 (2020) 21329–21337.
[50] T. Ouahrani, R.M. Boufatah, M. Benaissa, Á. Morales-García, M. Badawi, D. Errandonea, Phys. Rev. Mater. 7 (2023) 025403.
[51] R.A. Boto, J.P. Piquemal, J. Contreras-García, Revealing strong interactions with the reduced density gradient: a benchmark for covalent, ionic and charge-shift bonds, Theor. Chem. Acc. 136 (139) (2017) 2017.
[52] E.R. Johnson, S. Keinan, P. Mori-Sanchez, J. Contreras-Garcia, A.J. Cohen, W. Yang, Revealing noncovalent interactions, J. Am. Chem. Soc. 132 (2010) 6498–6506.